Applied Energy Science
https://www.sciltp.com/journals/aes

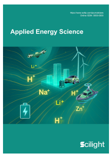

Article

N-Doped Chitin-Derived Porous Carbon Materials for Anodes of Potassium-Ion Batteries

Hua Qiu [1], Chuang Liu [1], Xianli Wu [1,*] and Xu Li [2]

[1] College of Chemistry, Zhengzhou University, Zhengzhou 450001, China
[2] Institute of Chemistry Henan Academy of Sciences & Henan Academy of Sciences, Zhengzhou 450000, China
* Correspondence: wuxianli@zzu.edu.cn

How To Cite: Qiu, H.; Liu, C.; Wu, X.; et al. N-Doped Chitin-Derived Porous Carbon Materials for Anodes of Potassium-Ion Batteries. *Applied Energy Science* **2026**, *1*(1), 3.

Received: 2 February 2026
Revised: 31 March 2026
Accepted: 10 April 2026
Published: 13 April 2026

Abstract: Potassium-ion batteries (PIBs) are considered a viable substitute for lithium-ion batteries owing to the natural abundance and inexpensive nature of potassium. However, their commercialization is impeded by challenges such as dendrite formation, significant volume expansion, slow ion diffusion, and the scarcity of suitable anode materials, while potassium metal anodes additionally face severe dendrite formation. In this work, to address these issues, a Chitin-derived nitrogen-doped porous carbon anode material (HC-3) with a large specific surface area and a mesoporous structure was prepared via $ZnCl_2$ chemical activation. When used as an anode for PIBs, the HC-3 performed a high reversible capacity of 257 mAh g^{-1} at 50 mA g^{-1} and outstanding cycling stability, retaining 240 mAh g^{-1} after 100 cycles. It also demonstrated superior rate capability, delivering capacities of 197, 133, 102, and 70 mAh g^{-1} at 100, 250, 500, and 1000 mA g^{-1}, respectively. Notably, when the current was reduced back to 50 mA g^{-1}, a capacity of 232 mAh g^{-1} was restored, demonstrating excellent structural reversibility. The superior electrochemical performance is ascribed to the synergistic effect of a hierarchical porous architecture and in-situ nitrogen doping, which facilitate K^+ transport kinetics, offer abundant active sites for K^+ storage, and accommodate volume changes. This work provides a sustainable and effective strategy for developing high-performance carbon anodes from biomass for next-generation energy storage systems.

Keywords: N-doped; Chitin-derived porous carbon; anode; potassium-ion batteries

1. Introduction

The escalating energy crisis has intensified the demand for developing next-generation battery technologies for large-scale energy storage, with stringent requirements for both cost efficiency and energy storage performance [1–3]. Commercially available lithium-ion batteries (LIBs) face challenges owing to the limited reserves and inhomogeneous geographical distribution of lithium resources, leading to continuously rising costs. In contrast, sodium and potassium, which belong to the same group as lithium, are far more abundant on Earth [4,5]. Given their chemical similarity to lithium, research interest has shifted toward sodium-ion batteries (SIBs) and potassium-ion batteries (PIBs) [6,7]. Over the past decade, more studies have focused on Na than on K, owing to its smaller atomic size. However, when graphite carbon materials are used as anodes in SIBs, only minimal Na^+ intercalation occurs due to the high formation energy of Na-graphite intercalation compounds, resulting in low reversible capacity and limiting commercial prospects [8,9]. Consequently, attention has turned to PIBs [10,11]. Interestingly, graphite anodes in PIBs deliver a reversible capacity comparable to that in LIBs [12]. Moreover, despite its larger ionic radius, K^+ exhibits higher ionic conductivity than Li^+ and Na^+ in liquid and polymer electrolytes due to its weaker Lewis acidity and lower desolvation energy, making PIBs a promising candidate for next-generation energy storage technologies [13,14].

Considerable efforts have been directed toward developing cathodes, anodes, and electrolytes for PIBs; however, their practical deployment continues to be restricted by the shortage of high-performance anode materials. Potassium metal anodes, despite their high theoretical capacity, suffer from severe dendrite formation and safety concerns, which necessitate the development of alternative anode materials. Carbonaceous materials, including those derived from biomass, offer a promising solution due to their stable porous structure and uniform ion flux, which can inherently mitigate dendrite-related risks [15–17]. Owing to its renewability, abundance, and environmental friendliness, biomass-derived carbon materials hold considerable promise. Following pretreatment steps such as washing and drying, the biomass is carbonized under an inert atmosphere (e.g., nitrogen or argon) at high temperatures (typically 400–900 °C) to yield biomass-derived carbon materials [18–20]. Recently, biomass carbon materials have been widely reported as anodes for PIBs. Various plant sources—including sugarcane, cyanobacteria, absorbent cotton, potatoes, and Ganoderma lucidum spores—have been utilized, yielding carbons with diverse potassium storage performances [21–25].

Processed animal-derived structures have also demonstrated good potassium storage performance [26,27]. Chitin, the second most abundant natural biomass on Earth, is primarily sourced from marine exoskeletons [28–34]. Its intrinsic nitrogen-rich functional groups enable in situ nitrogen self-doping during carbonization [35]. Previous studies have produced N-doped carbon nanofibers and cross-linked hierarchical porous N-doped carbon microspheres by direct carbonization of chitin, and these materials exhibit high reversible capacities as PIBs anodes. For instance, Hao et al. [36] converted Chitin biowaste into N-doped carbon nanofibers with high surface area and expanded interlayer spacing, demonstrating excellent reversible capacity. Similarly, hierarchical porous N-doped carbon microspheres have been obtained from crustacean Chitin via direct pyrolysis [37]. Natural Chitin-derived hard carbon from seafood waste shows high nitrogen content, significantly enhancing potassium storage performance [38]. The structure and composition of Chitin lead to varied potassium storage properties depending on the treatment method. Direct carbonization preserves its inherent fibrous network and enables in situ nitrogen doping; however, the resulting materials often exhibit limited reversible capacity, likely due to insufficient active sites for potassium storage [39]. Further modification to prepare porous carbons is therefore expected to improve electrochemical performance. Porous carbon materials possess rich pore structures, high specific surface area, and enhanced surface activity, which facilitate electrolyte wetting and K^+ transport, thereby improving potassium storage [40,41]. Physical and chemical activation are commonly employed to fabricate porous carbons [42]. Physical activation involves pyrolysis followed by treatment in an activating gas, where pores form via redox reactions [43]. Chemical activation entails co-pyrolysis of the precursor with chemical reagents under inert atmosphere, producing porous structures [44]. Owing to its low cost, high carbon yield, and ability to generate high-surface-area porous carbons, chemical activation is more frequently adopted. Among chemical activators, $ZnCl_2$ effectively dissolves biomass cellulose, reduces tar formation during pyrolysis, promotes aromatization, and creates abundant pore structures [45].

Although Chitin has been explored as a precursor for N-doped carbons in energy storage, its use specifically for chemically activated porous carbons—particularly with $ZnCl_2$—as PIB anodes remains scarcely reported. Most studies focus on direct carbonization or activation of other biomass sources. The combination of Chitin's inherent nitrogen content and fibrous morphology, together with $ZnCl_2$ activation to engineer a hierarchical porous structure, represents an underexplored strategy for developing high-performance anode materials.

In this work, we report a facile and sustainable route to synthesize N-doped mesoporous carbon from Chitin using $ZnCl_2$ chemical activation. We systematically investigate the effect of the Chitin/$ZnCl_2$ impregnation ratio on surface appearance, pore structure and potassium storage performance. When the impregnation ratio was 1:2, the specific capacity of the potassium-ion battery based on HC-3 as the anode material still remained at 240 mAh g^{-1} after cycling at 50 mA g^{-1} for 100 times, demonstrating excellent cycle stability. This method is designed to enhance the electrochemical performance of chitin-derived carbon as an anode for PIBs by exploiting the combined advantages of heteroatom doping and pore formation via chemical activation.

2. Experimental Section

2.1. Pretreatment of Chitin

All reagents were obtained from Macklin Reagent Co., Ltd. (Shanghai, China). A 5 g portion of commercial chitin was suspended in 100 g of 5 wt% KOH solution and agitated at 90 °C for 6 h. This alkali treatment was carried out four times to ensure complete removal of proteins. The resulting flocculent material was then processed for pigment removal by stirring in 200 g of a 50 wt% ethanol/water mixture for 48 h. After filtration, the product was rinsed thoroughly with deionized water, dried at 60 °C, and ground into a fine powder. The purified chitin was labeled as KC (KOH-treated chitin).

2.2. Preparation of Biomass Porous Carbon Materials

KC was employed as carbon precursor with $ZnCl_2$ as chemical activator. In a typical synthesis, varying amounts of $ZnCl_2$ (0.5, 0.75, 1, 1.25, and 1.5 g) were first dissolved in a dilute HCl solution (prepared by adding 5 drops of 37 wt% HCl to 50 mL deionized water) to create a weak acidic environment. Then, 0.5 g of KC was added to each solution to achieve different KC/$ZnCl_2$ impregnation ratios (1:1, 1:1.5, 1:2, 1:2.5, and 1:3 w/w).

The mixtures were homogenized in a constant-temperature water bath at 60 °C (500 rpm, 24 h), followed by vacuum filtration. The obtained solids were dried at 60 °C and ground into powder. Subsequently, carbonization was conducted in a tube furnace under N_2 atmosphere at 600 °C for 2 h, with a heating rate of 5 °C min^{-1}. The carbonized products were then soaked in 100 g of 7 wt% HCl solution for 24 h to eliminate residual Zn species, followed by repeated rinsing with deionized water until the pH reached neutrality. After final drying at 60 °C, the resulting porous carbon materials were designated as HC-1 to HC-5, corresponding to KC/$ZnCl_2$ ratios of 1:1, 1:1.5, 1:2, 1:2.5, and 1:3, respectively.

2.3. Characterization

The morphology and microstructure of the obtained materials were examined using scanning electron microscopy (SEM, SUPRA, Carl Zeiss, Oberkochen, Germany) and transmission electron microscopy (TEM, H-800, JEOL, Tokyo, Japan). Crystal structure characterization was performed on an X-ray powder diffractometer (XRD, D/max-2500B2+/PCX, Rigaku, Tokyo, Japan) with Cu K_α radiation (λ = 1.54056 Å), operating over a 2θ range of 10–70° at a scan rate of 10° min^{-1}. Raman spectroscopy (HR800, HORIBA Jobin Yvon, Palaiseau, France) was employed to evaluate the degree of structural disorder. X-ray photoelectron spectroscopy (XPS, ESCALAB 250, Thermo Fisher Scientific, Waltham, MA, USA) was utilized to analyze the binding energies of electrons, enabling qualitative and quantitative elemental analysis, solid surface characterization, and compound structure identification. In addition, the specific surface area and pore size distribution were determined using a BET surface area analyzer (AS-1C-VP, Micromeritics, Norcross, GA, USA).

2.4. Electrode Preparation and Electrochemical Measurements

The active material, Super P conductive additive, and polyvinylidene fluoride (PVDF) binder were mixed in a mass ratio of 8:1:1 through dry grinding. Subsequently, deionized water was added as a solvent, and the mixture was further wet-ground to form a homogeneous slurry with suitable viscosity. The resulting slurry was uniformly coated onto pre-dried copper foil and then dried in a vacuum oven at 120 °C for 10 h. The mass loading of active material on each electrode was approximately 1 mg cm^{-2}. Coin-type half-cells were assembled inside an argon-filled glove box (H_2O and O_2 levels below 0.1 ppm). The prepared electrode served as the working electrode, a potassium metal disk as the counter electrode, a Whatman GF/D cellulose membrane (16 mm diameter) as the separator, and 0.8 M KPF_6 dissolved in EC/DEC (1:1 by volume) as the electrolyte. Electrochemical testing was carried out on a Neware BTS series battery test system (CT-3008W-5V10mA-A4, Neware, Shenzhen, China). Cyclic voltammetry (CV) measurements were performed using a CS350 (Corrtes, Wuhan, China) electrochemical workstation over a voltage range of 0.01–3.0 V at a scan rate of 0.1 mV s^{-1}.

3. Results and Discussion

The synthesis strategy is illustrated in the Figure 1a. The synthesis begins by impregnating Chitin with $ZnCl_2$ to ensure uniform dispersion of the activator. During carbonization, $ZnCl_2$ is converted in situ to ZnO, which acts as a dispersed template for pore generation. Finally, HCl treatment selectively removes the ZnO template, creating a tailored porous architecture in the carbon. The micro-morphology and structure of the samples were analyzed by SEM and HRTEM shown as Figure 1b–e and Figure S1 (Supplementary Materials). It can be seen that Chitin can still retain its inherent fibrous morphology even after being activated by $ZnCl_2$. When the impregnation ratio is 1:2, as seen from the SEM images of HC-3, shown in Figure 1b,c, there are many pores between the fibers of Chitin after activation. Among the all of sample, the fibrous network structure of HC-3 is the most developed. These increased vacancies and gaps are beneficial to the transportation and adsorption of K^+ [19]. The HRTEM images in Figure 1d,e confirms that the porous carbon prepared after activation possesses a fibrous nanostructure with abundant pores, indicating that a KC/$ZnCl_2$ mass ratio of 1:2 can lead to a short-range ordered mesoporous structure. These structural features are beneficial for improving the potassium storage performance of the material [19]. In addition, selected area elemental mapping was performed on the HC-3 sample. Figure 1f–h shows the distribution of C, N, and O elements, respectively. The results confirm the successful in-situ N doping, and all three elements are uniformly distributed throughout the sample.

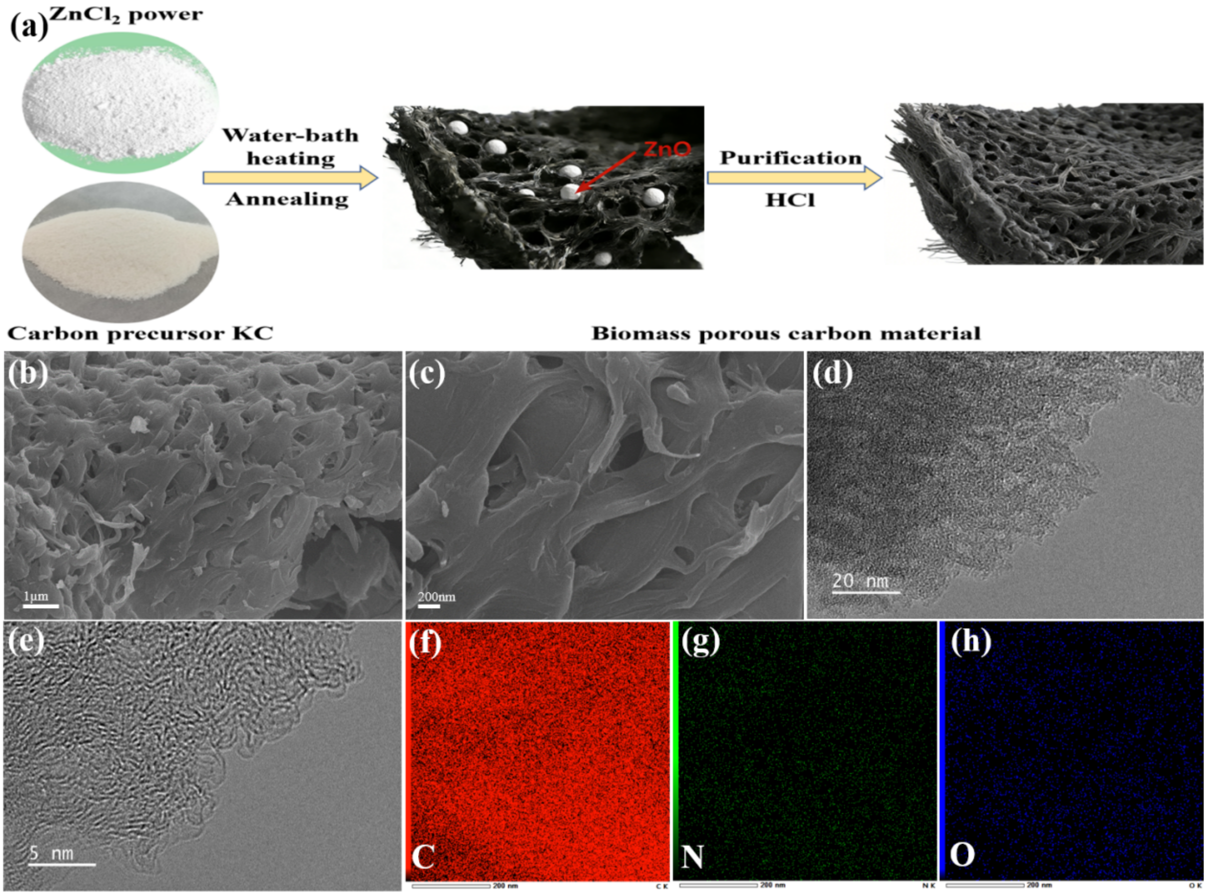

Figure 1. (**a**)Schematic of the preparation process for biomass porous carbon, (**b**,**c**) SEM, (**d**,**e**) TEM images and (**f**–**h**) Element mapping of C, N and O of HC-3.

XRD phase analysis was performed to identify the components of the sample and determine whether any inorganic impurities remained. Figure 2a displays the XRD patterns of HC-1, HC-2, HC-3, HC-4, and HC-5. It can be seen that the XRD curves of these five samples all have two broad diffraction peaks. The characteristic diffraction peak of the carbon material near 25° (002) shifts slightly to the left, and no other characteristic diffraction peaks are detected, demonstrating that the prepared materials are disordered hard carbons, and the chemical activator $ZnCl_2$ and other inorganic impurities generated during the carbonization process have been removed or only exist in negligible trace amounts. The diffraction peak of (100) is very weak and almost invisible, which indicates that the graphitization degree of these biomass carbon materials is extremely low [24]. The interplanar spacing of the (002) crystal plane was calculated by Bragg's law $2d\sin\theta = n\lambda$ ($\lambda = 1.54056$ Å). The d_{002} values of the five samples HC-1, HC-2, HC-3, HC-4, and HC-5 were calculated to be 3.72, 3.80, 3.89, 3.81, and 3.74 Å, respectively. These results demonstrate that $ZnCl_2$ activation effectively creates a porous carbon structure, simultaneously increasing accessible active sites for K^+ insertion/extraction and enhancing K^+ diffusion pathways through improved pore connectivity [45]. From the XRD results, it can be seen that when the mass of the activator $ZnCl_2$ is gradually increased, the interlayer spacing of the prepared carbon materials first increases and then decreases. When the mass ratio of KC to $ZnCl_2$ is 1:2 (sample HC-3), the interlayer spacing reaches the maximum of 3.89 Å, indicating that the mass ratio of 1:2 is the optimal impregnation ratio for the activation. Increasing the amount of $ZnCl_2$ may lead to the partial collapse of the pore structure formed in the subsequent carbonization process due to excessive pores. Raman spectroscopy analysis was conducted on the samples to measure the disorder degree of the carbon materials. Figure 2b shows the Raman spectra of five porous carbon samples. The Raman spectra of the samples are mainly characterized by a disordered D-band around ~1350 cm^{-1} and a graphitized G-band around ~1590 cm^{-1}. The calculated I_D/I_G ratios for HC-1 through HC-5 were determined to be 1.019, 1.027, 1.035, 1.034, and 1.024, respectively. HC-3 exhibits the highest ratio of I_D/I_G, indicating the greatest structural disorder among the samples. The $ZnCl_2$-activated porous carbons exhibit substantially higher I_D/I_G ratios (1.019–1.035) compared to pristine graphite (~0.9) [46], confirming the effectiveness of chemical activation in simultaneously introducing abundant porosity and increasing structural disorder within the carbon matrix. This provides more active sites for the adsorption of K^+ and is beneficial for improving the potassium-storage performance of the materials [19]. The evolution of interlayer spacing and I_D/I_G ratio with increasing $ZnCl_2$ loading follows a volcano-shaped trend. The initial increase is attributed to the introduction of defects and lattice expansion by moderate $ZnCl_2$ activation, which creates active sites and pore precursors. However, excessive $ZnCl_2$ (ratios beyond 1:2) leads to over-activation, causing partial pore wall collapse and localized graphitic ordering, which reduces both the interlayer spacing and the degree of disorder. These structural changes, as evidenced by XRD and Raman analysis, provide a clear mechanistic understanding of the $ZnCl_2$ activation process and its effect on the pore structure evolution.

The pore structure of HC-3 was investigated by N_2 adsorption-desorption measurements, with the corresponding isotherm presented in Figure 2c. HC-3 exhibits the IV type curves according to the IUPAC and BDDT classification. The obvious hysteresis loop shows that the prepared carbon material has a rich mesoporous structure. Pore size distribution was derived from the BJH method. HC-3 exhibited a BET specific surface area of 280.7 $m^2\ g^{-1}$ and an average pore diameter of 4.3 nm. The higher specific surface area and mesoporous structure will accelerate the adsorption and rapid diffusion of K^+ and is beneficial for improving the rapid charge—discharge performance of the material [22].

XPS analysis were carried out to detect surface elements and electric structure. The survey spectrum in Figure S2 (Supplementary Materials) indicates that only three elements, C, O, and N, are on the surface of sample. The atomic percentages of C, O, and N are 84.88, 9.30, and 5.82 at%, respectively. As shown in Figure 2d, the C 1s XPS fine spectrum of the HC-3 sample contains four independent component peaks, including the C-C bond at 284.5 eV, the C-O bond at 285.5eV, the C-N bond at 286.5 eV, and the C-C=O bond at 289.5 eV [47]. The N 1s spectrum can be divided into four main peaks, located at 398.4 eV, 399.5 eV, 400.8 eV, and 402.09 eV in Figure 2e, respectively, corresponding to pyridinic nitrogen (N6), pyrrolic nitrogen (N5), quaternary nitrogen (N-Q), and pyridinic N-oxide (N-O_X) [28]. Pyridinic N (N-6) enhances electronic conductivity and increases K^+ adsorption energy at edge sites, facilitating charge transfer [36,47]. Pyrrolic N (N-5) introduces topological defects that create additional nanopores for K^+ storage and help buffer volume strain, improving structural stability [28,38]. Their synergy enhances both capacity and cyclability. Moreover, quaternary nitrogen can enhance the electrical conductivity of the material, which is beneficial for accelerating the K^+ electron transfer process during the charging/discharging process [34]. The O 1s spectrum in Figure 2f clearly shows the presence of three oxygen-containing functional groups, including C-O (530.8 eV), O-H (531.9 eV), and C=O (533.2 eV) [28], all of which have a positive impact on the electrochemical performance of the material.

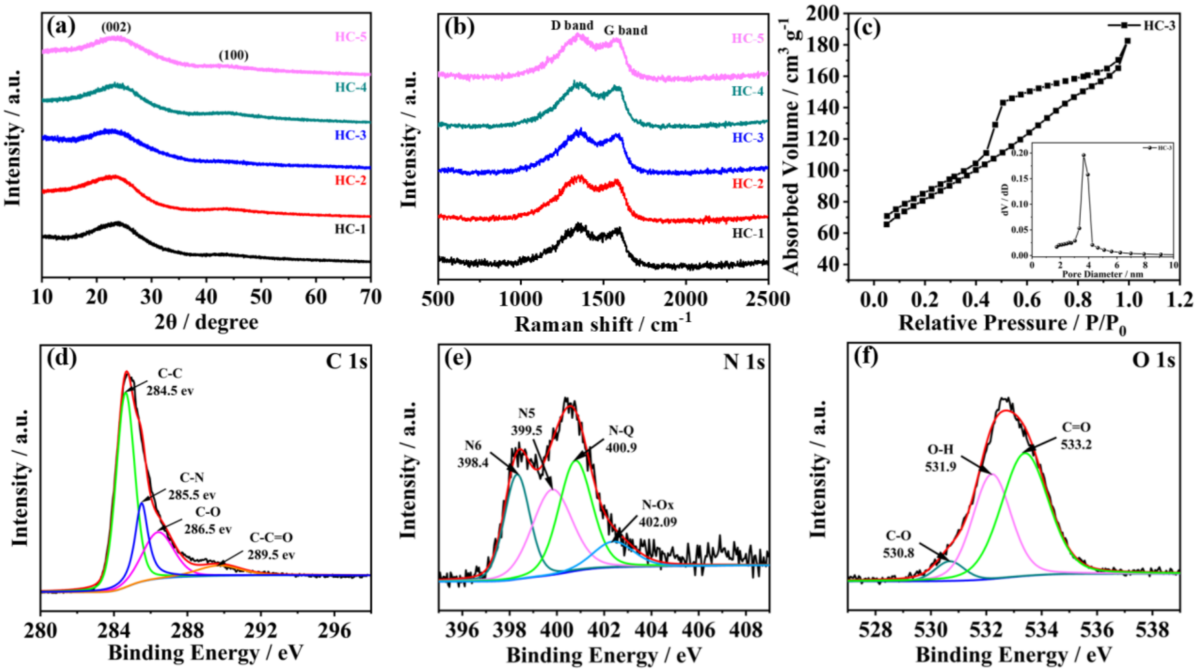

Figure 2. (**a**) XRD patterns and (**b**) Raman spectra of HC-1, HC-2, HC-3, HC-4 and HC-5, (**c**) N_2 adsorption-desorption isotherms, pore-size distributions and XPS (**d**) C 1s, (**e**) N 1s, (**f**) O 1s spectra of HC-3.

To assess the potential of the prepared carbon materials as anode materials for PIBs, the electrochemical performance of the prepared materials was evaluated through cycle testing, rate capability measurements, and cyclic voltammetry (CV). The cycling results at a current density of 50 mA g^{-1} are presented in Figure 3a. After 100 cycles, HC-1, HC-2, HC-3, HC-4, and HC-5 delivered remaining specific capacities of 182, 210, 240, 214, and 176 mAh g^{-1}, respectively. HC-3 demonstrated the highest cycle performance owing to an optimal impregnation ratio of 1:2 in preparation. Insufficient ratio led to poor activation, while excessive ratio wasted activator and allowed excess $ZnCl_2$ to disrupt the fibrous structure, degrading electrochemical performance [45]. Figure 3b shows that HC-3, when used as an anode for PIBs, retains a reversible capacity of 177.8 mAh g^{-1} after 500 cycles at a current density of 50 mA g^{-1}, corresponding to 71.72% of the initial capacity after stabilization. For HC-3 as a PIB anode, the initial charge and discharge capacities were 272 and 819 mAh g^{-1}, respectively, with an initial Coulombic efficiency of 33.2%. The low initial Coulombic efficiency (ICE) is primarily attributed to the irreversible formation of a solid electrolyte interphase (SEI) on the high-surface-area porous carbon and irreversible reactions between K^+ and surface functional groups (e.g., C=O, N species) during the first discharge [19,38]. This process does not compromise long-term stability. A stable SEI forms after the first cycle, enabling highly reversible cycling, as evidenced by the near 100% Coulombic efficiency thereafter. The rate performance diagram of the samples at different current densities showed the HC-3 sample has the best rate performance in Figure 3c. When the current densities are 50, 100, 250, 500, and 1000 mA g^{-1}, the specific capacities of the HC-3 sample are 257, 197, 133, 102, and 70 mAh g^{-1}, respectively. To benchmark the electrochemical performance of HC-3 against previously reported biomass-derived carbon anodes for PIBs, a comparison is summarized in Table 1. HC-3 demonstrates superior reversible capacity and rate capability, particularly when compared to chitin-derived carbons prepared by direct carbonization.

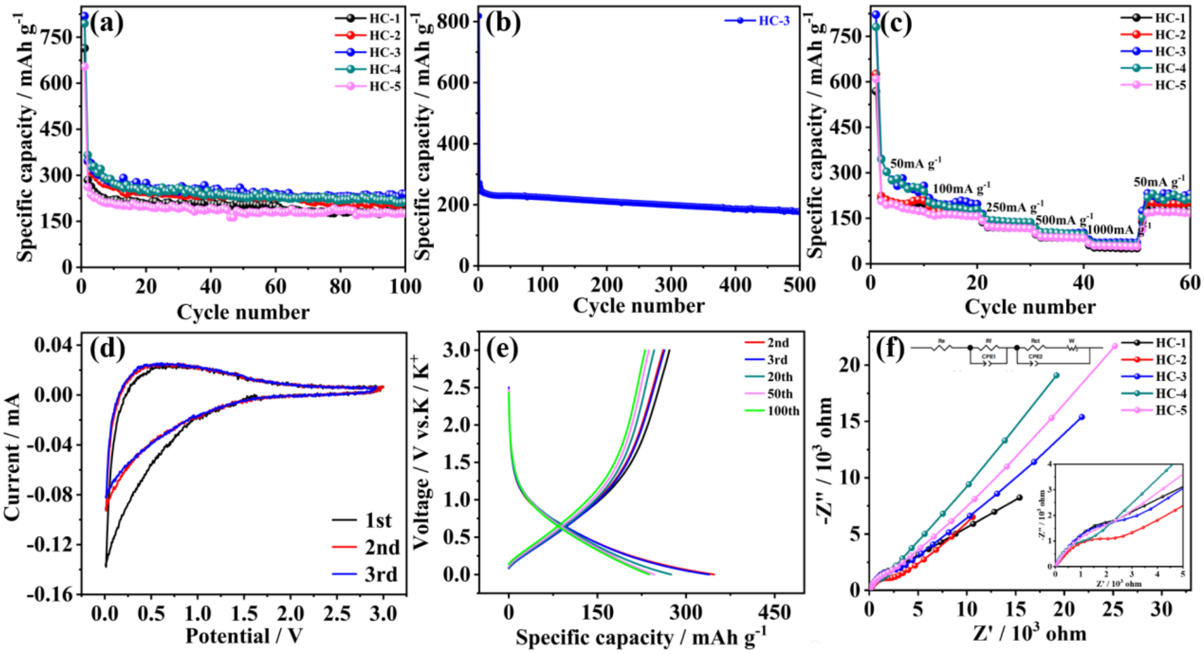

Figure 3. (**a**,**b**) Cycle performance at a current density of 50 mA g^{-1}, (**c**) rate performance under different current densities and (**d**) the CV curve of the first three circles at a sweep rate of 0.1 mV s^{-1}, (**e**) the charge-discharge curve, (**f**) AC impedance spectra and fitting circuit of the HC-3 for PIBs anode.

Figure 3d shows the CV curve of HC-3 measured at a scanning rate of 0.1 mV s^{-1}. The broad peak observed below 1 V during the first cycle corresponds to SEI film formation. The reduction peak at 0.01 V and the oxidation peak near 0.5 V correspond to the insertion and extraction of K^+, respectively [20]. As observed in Figure 3e, the charge/discharge profiles exhibit a near-linear shape without distinct voltage plateaus. This suggests a primarily capacitive, rather than diffusion-controlled, energy storage mechanism in the biomass-derived carbon anode [48]. Meanwhile, the charge-discharge curves of the 20th, 50th, and 100th cycles overlap significantly, indicating that the HC-3 sample has good cycle stability. Among all the samples, HC-3 exhibited the best cycling stability and rate capability. This superior electrochemical performance is attributed to its tailored porous structure, which was achieved using an optimal Chitin/$ZnCl_2$ impregnation ratio of 1:2 during chemical activation.

Table 1. Comparison of electrochemical performance of HC-3 with previously reported biomass-derived carbon anodes for PIB.

Material	Precursor	SSA ($m^2\ g^{-1}$)	N Content (at%)	Current Density ($mA\ g^{-1}$)	Reversible Capacity ($mAh\ g^{-1}$)	Cycling Stability	Rate Capability ($mAh\ g^{-1}$)
HC-3	Chitin	280.7	5.82	50	240 (after 100 cycles)	71.7% after 500 cycles	197 (100 mA g^{-1}), 133 (250), 102 (500), 70 (1000)
N-doped carbon nanofibers [36]	Chitin	120	4.5	50	~180 (after 100 cycles)	~85% after 100 cycles	~150 (100 mA g^{-1}), ~100 (500)
N-rich hard carbon [38]	Chitin (shrimp shell)	350	6.1	50	~210 (after 100 cycles)	~88% after 200 cycles	~160 (100 mA g^{-1}), ~110 (500)
N-doped porous carbon [28]	Chitin	/	/	50	~190 (after 100 cycles)	~80% after 100 cycles	~140 (100 mA g^{-1})
N-doped carbon [20]	Walnut septum	400	3.2	50	~200 (after 100 cycles)	~90% after 100 cycles	~150 (100 mA g^{-1}), ~100 (500)
Porous carbon [24]	Potato	580	/	50	~210 (after 100 cycles)	~85% after 100 cycles	~160 (100 mA g^{-1}), ~110 (500)
N-doped carbon [19]	Corn husk	450	2.8	50	~190 (after 100 cycles)	~83% after 100 cycles	~140 (100 mA g^{-1})
Hard carbon [23]	Skimmed cotton	520	/	50	~200 (after 100 cycles)	~88% after 100 cycles	~150 (100 mA g^{-1})

SSA: specific surface area; "/" indicates data not available in the original reference.

EIS measurements were conducted on all five samples (HC-1 to HC-5) after 10 cycles at a current density of 500 mA g^{-1} in PIB half-cells. The Nyquist plots along with the corresponding equivalent circuit are presented in Figure 3f. The fitted charge-transfer resistance (R_{ct}) values for HC-1, HC-2, HC-3, HC-4, and HC-5 are 1685, 1459.6, 528.65, 1024.2, and 2015.3 Ω, respectively. HC-3 exhibits the lowest R_{ct}, indicating the highest electrical conductivity among the samples. This result further confirms that the KC/$ZnCl_2$ impregnation ratio of 1:2 is optimal for the chemical activation of chitin-derived porous carbon, leading to superior electrochemical kinetics.

Employing kinetic analysis of CV to deconvolute the contributions of diffusion-controlled processes (pseudo-capacitance) and surface-controlled processes (non-faradaic electric double-layer capacitance and surface faradaic pseudo-capacitance) represents an advanced approach for evaluating the performance of electrode materials [47]. The CV curves of PIBs based on the HC-3 anode, recorded at scanning rates of 0.2, 0.4, 0.6, 0.8, and 1.0 mV s^{-1}, are displayed in Figure 4a. The contribution from surface capacitive behavior can be qualitatively assessed using the relationship $i = av^b$, which links the peak current (i) from CV curves to the scan rate (v), where a and b are constants. Here, b represents the slope of the log(i) versus log(v) plot, and typically falls within the range of 0.5 to 1. When b = 1, it indicates that the process is completely controlled by the surface capacitive behavior. When b = 0.5, it means that the process is completely controlled by the diffusion behavior. When b is between 0.5 and 1, it represents a mixed control mechanism [8,9]. As shown in Figure 4b, the b values for the cathodic and anodic peaks of HC-3 are determined to be 0.67 and 0.76, respectively, demonstrating that the process is jointly controlled by two mechanisms. For a quantitative analysis of the two reaction behaviors, surface-capacitive behavior can be deconvoluted from the total current via data processing and calculation. The shaded area in Figure 4c corresponds to the capacitive contribution at a scan rate of 0.8 mV s^{-1}, constituting 73.65% of the total current. The contribution proportion of the capacitive behavior can be further determined by the formula $i(V) = k_1 v + k_2 v^{1/2}$, where k_1 and k_2 are variable parameters. The contribution ratios of the capacitive behavior at different scanning rates were determined through fitting calculations, and the results are shown in Figure 4d. The results show that when the scanning rates are 0.2, 0.4, 0.6, 0.8, and 1.0 mV s^{-1}, the contribution ratios of the capacitive behavior are 47.5%, 54.97%, 64.32%, 73.65% and 80.53%, respectively. When the scanning rate is low, the process is more controlled by diffusion. With increasing scan rate, the contribution associated with surface-controlled capacitive processes grows more pronounced. The capacitive process can promote the rapid diffusion of ions and maintain the structural stability, which is beneficial for improving the potassium storage performance of the material [47].

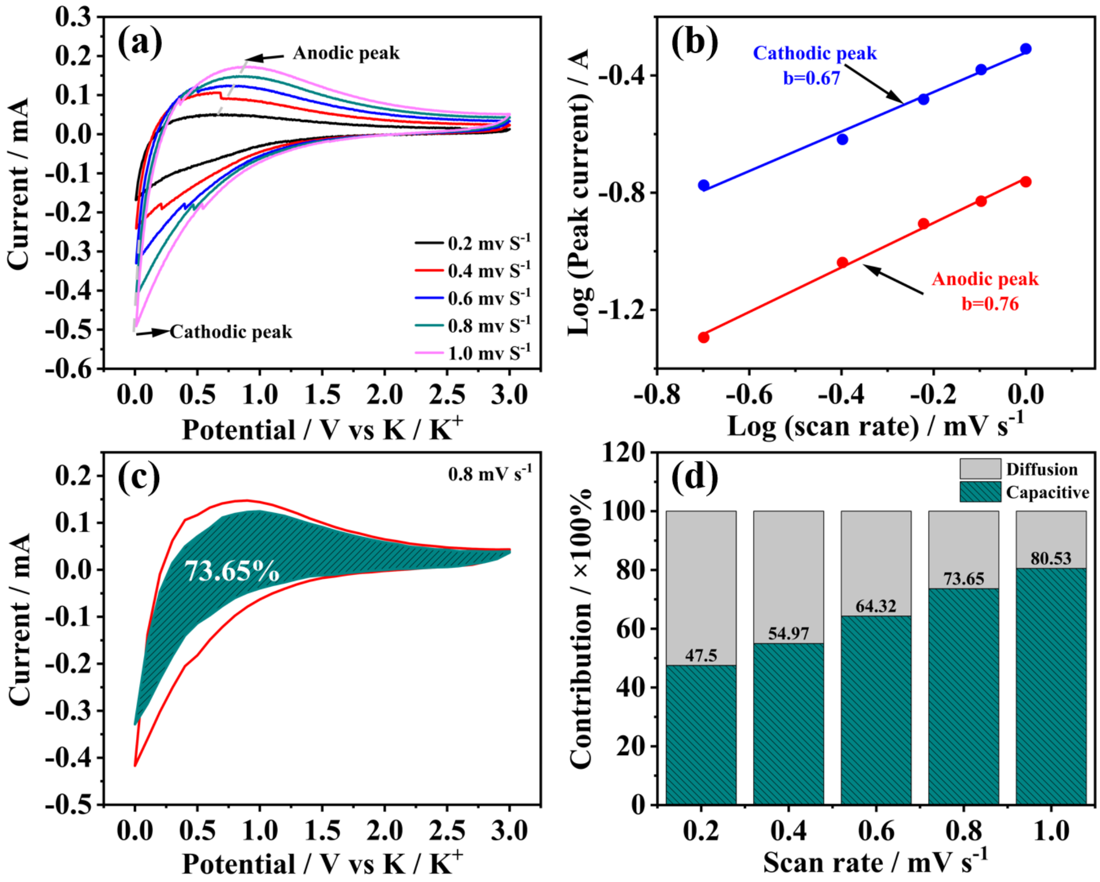

Figure 4. (**a**) CV curves of HC-3 as an anode for PIBs at scan rates of 0.2, 0.4, 0.6, 0.8, and 1.0 mV s^{-1}; (**b**) plot of b values as a function of scan rate for the cathodic and anodic peaks; (**c**) separation of total current (solid line) into capacitive current (dashed line) at a scan rate of 0.8 mV s^{-1}; (**d**) capacitive and diffusion contributions at various scan rates.

4. Conclusions

In this work, a Chitin-derived nitrogen-containing porous carbon material was successfully prepared by using KC as the carbon precursor and $ZnCl_2$ as the chemical activator. When the mass ratio of the KC to $ZnCl_2$ is 1:2, the porous carbon material, HC-3, exhibits the best electrochemical performance. When HC-3 was used as the anode of PIBs, a specific capacity of 240 mA g^{-1} can be retained after cycled 100 times at a current density of 50 mA g^{-1}. Furthermore, the material demonstrates excellent rate capability, maintaining a reversible capacity of 232 mAh g^{-1} upon returning the current density to 50 mA g^{-1} after high-rate cycling. This robust performance is attributed to the well-developed mesoporous structure and the increased defects/vacancies introduced by $ZnCl_2$ activation. The porous framework facilitates rapid K^+ transport, while the enhanced defect density provides abundant active sites for K^+ adsorption. The relatively low ICE (33.2%) of HC-3 stems from its large specific surface area and numerous structural imperfections, which promote extensive SEI formation. To address this limitation, future work could focus on pre-potassiation treatments (chemical or electrochemical), surface coating with a thin protective layer (e.g., carbon or TiO_2), or electrolyte optimization (e.g., using FEC additive) to minimize irreversible capacity loss and enhance ICE, thereby improving the practical viability of the material.

Supplementary Materials

The additional data and information can be downloaded at: https://media.sciltp.com/articles/others/2604131009077044/AES-26020011-SM.pdf. Figure S1: SEM images of (a) HC-1; (b) HC-2; (c) HC-4; (d) HC-5 and TEM images of (e) HC-2, (f) HC-4. Figure S2: XPS survey spectrum of HC-3.

Author Contributions

H.Q.: Conceptualization, methodology, investigation, data curation, writing—original draft preparation, visualization. C.L.: Methodology, investigation, formal analysis, data curation. X.W.: Conceptualization, resources, supervision, writing—review and editing, project administration, funding acquisition. X.L.: Resources, validation, writing—review and editing. All authors have read and approved the final version of the manuscript and agree to be personally accountable for their own contributions and for ensuring the accuracy and integrity of the work.

Funding

This research was funded by Joint Fund of Henan Province Science and Technology R&D Program (235200810027), Henan Provincial Key R&D and Promotion Special (Science and Technology Tackling) Project (242102230180), Henan Provincial Natural Science Foundation General Project (242300420193), High-level Talent Research Start-up Project Funding of Henan Academy of Sciences (232018002), The Fundamental Research Fund of Henan Academy of Sciences (20250603005), The Scientific and Technological Research Project of Henan Academy of Sciences (20252303002).

Institutional Review Board Statement

Not applicable.

Informed Consent Statement

Not applicable.

Data Availability Statement

The raw data supporting the conclusions of this article, including the original SEM, TEM, XRD, XPS, Raman, BET, and electrochemical measurements, have not been deposited in a public repository because of the large file sizes and the specific format requirements. However, all data are available from the corresponding author upon reasonable request. The authors commit to preserving the data for at least 10 years after publication.

Conflicts of Interest

The authors declare no conflict of interest.

Use of AI and AI-Assisted Technologies

No AI tools were utilized for this paper.

References

1. Rehman, J.; Fan, X.F.; Laref, A.; et al. Potential anodic applications of 2D MoS_2 for K-ion batteries. *J. Alloys Compd.* **2021**, 865, 158782.
2. Sang, Z.Y.; Su, D.; Wang, J.S.; et al. Bi-continuous nanoporous carbon sphere derived from SiOC as high-performance anodes for PIBs. *Chem. Eng. J.* **2020**, 381, 122677.
3. Xiong, W.; Zhang, J.Q.; Xiao, Y.; et al. Oxygen-rich nanoflake-interlaced carbon microspheres for potassium-ion battery anodes. *Chem. Commun.* **2020**, 56, 3433–3436.
4. Tao, X.S.; Sun, Y.G.; Liu, Y.; et al. Facile synthesis of hollow carbon nanospheres and their potential as stable anode materials in potassium-ion batteries. *ACS Appl. Mater. Interfaces* **2020**, 12, 13182–13188.
5. Yang, Y.L.; Li, D.; Zhang, J.Q.; et al. Sn nanoparticles anchored on N doped porous carbon as an anode for potassium ion batteries. *Mater. Lett.* **2019**, 256, 126613.
6. Bai, L.; Liu, Q.; Hong, T.; et al. Defect-rich N/O-co-doped porous carbon frameworks as anodes for superior potassium and sodium-ion batteries. *New Carbon Mater.* **2024**, 39, 1144–1156.
7. Kim, H.; Kim, J.C.; Bianchini, M.; et al. Recent progress and perspective in electrode materials for K-ion batteries. *Adv. Energy Mater.* **2017**, 8, 1702384.
8. Pan, E.Z.; Jin, Y.H.; Zhao, C.C.; et al. Mesoporous Sn_4P_3-graphene aerogel composite as a high-performance anode in sodium ion batteries. *Appl. Surf. Sci.* **2019**, 475, 12–19.
9. Pan, E.Z.; Jin, Y.H.; Zhao, C.C.; et al. Conformal hollow carbon sphere coated on Sn_4P_3 microspheres as high-rate and cycle-stable anode materials with superior sodium storage capability. *ACS Appl. Energy Mater.* **2019**, 2, 1756–1764.
10. Tan, H.; Du, X.Q.; Zhou, R.; et al. Rational design of microstructure and interphase enables high-capacity and long-life carbon anodes for potassium ion batteries. *Carbon* **2021**, 176, 383–389.
11. Wang, X.J.; Ma, J.Y.; Wang, J.M.; et al. N-doped hollow carbon nanofibers anchored hierarchical FeP nanosheets as high-performance anode for potassium-ion batteries. *J. Alloys Compd.* **2020**, 821, 153268.

12. Wang, W.; Zhou, J.H.; Wang, Z.P.; et al. Short-range order in mesoporous carbon boosts potassium-ion battery performance. *Adv. Energy Mater.* **2018**, 8, 1701648.
13. Pan, Q.; Li, B.; Liu, S.; et al. Flower-like graphitic carbon derived from biomass for anode of potassium ion battery. *Chem. Eng. Sci.* **2025**, 304, 121043.
14. Cheng, L.; Quan, J.; Li, H. Recent advances in antimony-based anode materials for potassium-ion batteries: Material selection, structural design and storage mechanisms. *Chin. Chem. Lett.* **2025**, 36, 110685.
15. Hou, H.S.; Qiu, X.Q.; Wei, W.F.; et al. Carbon anode materials for advanced sodium-ion batteries. *Adv. Energy Mater.* **2017**, 7, 1602898.
16. Li, H.Y.; Cheng, Z.; Zhang, Q.; et al. Bacterial-derived, compressible, and hierarchical porous carbon for high-performance potassium-ion batteries. *Nano Lett.* **2018**, 18, 7407–7413.
17. Jiang, H.J.; Huang, L.; Wei, Y.H.; et al. Bio-derived hierarchical multicore-shell Fe_2N-nanoparticle-impregnated N-doped carbon nanofiber bundles: A host material for lithium/potassium-ion storage. *Nano-Micro Lett.* **2019**, *11*, 56.
18. Cui, R.C.; Xu, B.; Dong, H.J.; et al. N/O dual-doped environment-friendly hard carbon as advanced anode for potassium-ion batteries. *Adv. Sci.* **2020**, *7*, 1902547.
19. Wang, Q.; Gao, C.L.; Zhang, W.X.; et al. Biomorphic carbon derived from corn husk as a promising anode materials for potassium ion battery. *Electrochim. Acta* **2019**, *324*, 134902.
20. Gao, C.L.; Wang, Q.; Luo, S.H.; et al. High performance potassium-ion battery anode based on biomorphic N-doped carbon derived from walnut septum. *J. Power Sources* **2019**, *415*, 165–171.
21. Yang, T.Z.; Qian, T.; Wang, M.F.; et al. A sustainable route from biomass byproduct okara to high content nitrogen-doped carbon sheets for efficient sodium ion batteries. *Adv. Mater.* **2016**, *28*, 539–545.
22. Zhang, Z.L.; Jia, B.R.; Liu, L.; et al. Hollow multihole carbon bowls: A stress-release structure design for high-stability and high-volumetric-capacity potassium-ion batteries. *ACS Nano* **2019**, *13*, 11363–11371.
23. He, X.D.; Liao, J.Y.; Tang, Z.F.; et al. Highly disordered hard carbon derived from skimmed cotton as a high-performance anode material for potassium-ion batteries. *J. Power Sources* **2018**, *396*, 533–541.
24. Cao, W.; Zhang, E.J.; Wang, J.; et al. Potato derived biomass porous carbon as anode for potassium ion batteries. *Electrochim. Acta* **2019**, *293*, 364–370.
25. Yang, M.M.; Dai, J.Y.; He, M.Y.; et al. Biomass-derived carbon from Ganoderma lucidum spore as a promising anode material for rapid potassium-ion storage. *J. Colloid Interface Sci.* **2020**, *567*, 256–263.
26. Xu, B.L.; Qi, S.H.; Li, F.; et al. Cotton-derived oxygen/sulfur co-doped hard carbon as advanced anode material for potassium-ion batteries. *Chin. Chem. Lett.* **2019**, *31*, 217–222.
27. Yang, M.M.; Kong, Q.Q.; Feng, W.; et al. N/O double-doped biomass hard carbon material realizes fast and stable potassium ion storage. *Carbon* **2021**, *176*, 71–82.
28. Gao, L.F.; Ma, J.Q.; Li, S.P.; et al. 2D ultrathin carbon nanosheets with rich N/O content constructed by stripping bulk chitin for high-performance sodium ion batteries. *Nanoscale* **2019**, *11*, 12626–12636.
29. Stephan, A.M.; Kumar, T.P.; Kulandainathan, M.A.; et al. Chitin-incorporated poly (ethylene oxide)-based nanocomposite electrolytes for lithium batteries. *J. Phys. Chem. B* **2009**, *113*, 1963–1971.
30. Hao, R.; Yang, Y.; Wang, H.; et al. Direct chitin conversion to N-doped amorphous carbon nanofibers for high-performing full sodium-ion batteries. *Nano Energy* **2018**, *45*, 220–228.
31. Hu, M.X.; Yang, L.; Zhou, K.; et al. Enhanced sodium-ion storage of nitrogen-rich hard carbon by NaCl intercalation. *Carbon* **2017**, *122*, 680–686.
32. Kim, J.K.; Kim, D.H.; Joo, S.H.; et al. Hierarchical chitin fibers with aligned nanofibrillar architectures: A nonwoven-mat separator for lithium metal batteries. *ACS Nano* **2017**, *11*, 6114–6121.
33. Zhang, T.W.; Shen, B.; Yao, H.B.; et al. Prawn shell derived chitin nanofiber membranes as advanced sustainable separators for Li/Na-ion batteries. *Nano Lett.* **2017**, *17*, 4894–4901.
34. Li, J.; Luo, F.L.; Lin, T.; et al. Pomelo peel-based N, O-codoped hierarchical porous carbon material for supercapacitor application. *Chem. Phys. Lett.* **2020**, *753*, 137597.
35. Wang, M.; Ma, J.; Yang, H.Q.; et al. Nitrogen and cobalt Co-coped carbon materials derived from biomass chitin as high-performance electrocatalyst for aluminum-air batteries. *Catalysts* **2019**, *9*, 954.
36. Hao, R.; Lan, H.; Kuang, C.W.; et al. Superior potassium storage in chitin-derived natural nitrogen-doped carbon nanofibers. *Carbon* **2018**, *128*, 224–230.
37. Jo, D.Y.; Park, S.K. Facile Fabrication of Porous $MoSe_2$/Carbon Microspheres via the Aerosol Process as Anode Materials in Potassium-Ion Batteries. *Batteries* **2024**, *10*, 13.
38. Chen, C.J.; Wang, Z.G.; Zhang, B.; et al. Nitrogen-rich hard carbon as a highly durable anode for high-power potassium-ion batteries. *Energy Storage Mater.* **2017**, *8*, 161–168.
39. Zhu, L.F.; Zhang, Z.; Luo, J.D.; et al. Self-templated synthesis of hollow hierarchical porous olive-like carbon toward universal high-performance alkali (Li, Na, K)-ion storage. *Carbon* **2020**, *174*, 317–324.

40. Wang, H.H.; Artemova, A.; Yang, G.; et al. Lotus root-like porous carbon for potassium ion battery with high stability and rate performance. *J. Power Sources* **2020**, *466*, 228303.
41. Zhao, W.Q.; Shen, Y.P.; Zhang, H.; et al. Porous-carbon aerogels with tailored sub-nanopores for high cycling stability and rate capability potassium-ion battery anodes. *ACS Appl. Mater. Interfaces* **2020**, *12*, 27045–27054.
42. Yu, K.F.; Liu, T.; Zhang, Q.G.; et al. Rice husk lignin-based porous carbon and ZnO composite as an anode for high-performance lithium-ion batteries. *ACS Appl. Mater. Interfaces* **2020**, *27*, 875–882.
43. Meng, S.J.; Mo, Z.L.; Li, Z.L.; et al. Oxygen-rich porous carbons derived from alfalfa flowers for high performance supercapacitors. *Mater. Chem. Phys.* **2020**, *246*, 122830.
44. Yang, C.H.; Xiong, J.W.; Ou, X.; et al. A renewable natural cotton derived and nitrogen/sulfur co-doped carbon as a high-performance sodium ion battery anode. *Mater. Today Energy* **2018**, *8*, 37–44.
45. Choi, S.H.; Baucom, J.; Li, X.R.; et al. Porous carbon microspheres with highly graphitized structure for potassium-ion storage. *J. Colloid Interface Sci.* **2020**, *577*, 48–53.
46. An, Y.L.; Fei, H.F.; Zeng, G.F.; et al. Commercial expanded graphite as a low-cost, long-cycling life anode for potassium-ion batteries with conventional carbonate electrolyte. *J. Power Sources* **2018**, *378*, 66–72.
47. Xia, X.H.; Chao, D.L.; Zhang, Y.Q.; et al. Generic Synthesis of Carbon Nanotube Branches on Metal Oxide Arrays Exhibiting Stable High-Rate and Long-Cycle Sodium-Ion Storage. *Small* **2016**, *12*, 3048–3058.
48. Sultana, I.; Rahman, M.; Mateti, S.; et al. K-ion and Na-ion storage performances of Co_3O_4-Fe_2O_3 nanoparticle-decorated super P carbon black prepared by a ball milling process. *Nanoscale* **2017**, *9*, 3646–3654.